

Gate control of Mott metal-insulator transition in a 2D metal-organic framework

Benjamin Lowe^{1,2†}, Bernard Field^{1,2†}, Jack Hellerstedt^{1,2}, Julian Ceddia^{1,2}, Henry L. Nourse³, Ben J. Powell^{4*}, Nikhil V. Medhekar^{2,5*} and Agustin Schiffrin^{1,2*}

¹School of Physics and Astronomy, Monash University, Clayton, Victoria 3800, Australia.

²ARC Centre of Excellence in Future Low-Energy Electronics Technologies, Monash University, Clayton, Victoria 3800, Australia.

³Quantum Information Science and Technology Unit, Okinawa Institute of Science and Technology Graduate University, Onna-son, Okinawa 904-0495, Japan.

⁴School of Mathematics and Physics, The University of Queensland, Brisbane, Queensland 4072, Australia.

⁵Department of Materials Science and Engineering, Monash University, Clayton, Victoria 3800, Australia.

*Corresponding author(s). E-mail(s): powell@physics.uq.edu.au; nikhil.medhekar@monash.edu; agustin.schiffrin@monash.edu;

†These authors contributed equally to this work.

Abstract

Strong electron-electron Coulomb interactions in materials can lead to a vast range of exotic many-body quantum phenomena, including Mott metal-insulator transitions, magnetic order, quantum spin liquids, and unconventional superconductivity. These many-body phases are strongly dependent on band occupation and can hence be controlled via the chemical potential. Flat electronic bands in two-dimensional (2D) and layered materials such as the kagome lattice, enhance strong electronic correlations. Although theoretically predicted, correlated-electron phases in monolayer 2D metal-organic frameworks (MOFs) – which benefit from efficient synthesis protocols and tunable properties – with a kagome

2 Gate Control of Mott MIT in a 2D MOF

structure have not yet been realised experimentally. Here, we synthesise a 2D kagome MOF comprised of 9,10-dicyanoanthracene molecules and copper atoms on an atomically thin insulator, monolayer hexagonal boron nitride (hBN) on Cu(111). Scanning tunnelling microscopy (STM) and spectroscopy reveal an electronic energy gap of ~ 200 meV in this MOF, consistent with dynamical mean-field theory predictions of a Mott insulating phase. By tuning the electron population of kagome bands, via either template-induced (via local work function variations of the hBN/Cu(111) substrate) or tip-induced (via the STM probe) gating, we are able to induce Mott metal-insulator transitions in the MOF. These findings pave the way for devices and technologies based on 2D MOFs and on electrostatic control of many-body quantum phases therein.

Keywords: Strongly correlated electrons, metal-organic frameworks, kagome, dynamical mean-field theory, scanning probe microscopy, Mott insulator, metal-insulator transition

Strong electronic correlations arise in a material at specific electron fillings of its bands, provided that the on-site Coulomb repulsion (characterised by the Hubbard energy, U) is of the order of or larger than the bandwidth, W . These electronic correlations can result in a wide range of exotic many-body quantum phases. Examples include correlated insulating phases, quantum spin liquids (QSL), correlated magnetism, and superconductivity – phenomena which have been realised in monolayer transition metal-dichalcogenides [1–6], twisted few-layer graphene [7, 8], inorganic kagome crystals [9–11], and organic charge transfer salts [12–14].

Tuning of the chemical potential via electrostatic gating can allow for control over such band electron filling, enabling reversible switching between correlated phases [7]. This makes these systems amenable to integration as active materials in voltage-controlled devices, offering enticing prospects for applications in electronics, spintronics, and information processing and storage [12, 15].

Two-dimensional (2D) materials have emerged as particularly promising candidates for realising strongly correlated phenomena as the absence of inter-layer hopping and screening can contribute to decreasing W and increasing U [4]. Additionally, some 2D crystal geometries – such as the kagome structure – give rise to intrinsic flat electronic bands [16, 17]. When these bands of extremely narrow W are half-filled, even weak Coulomb repulsion can open an energy gap and give rise to a Mott insulating phase [12]. Away from half-filling, the gap closes and the system becomes metallic.

Metal-organic frameworks (MOFs) are a broad class of materials whose properties are highly tunable through careful selection of constituent organic molecules and metal atoms [18]. There has been growing interest in 2D MOFs for their electronic [19–21] and magnetic properties [22, 23], including strongly correlated phases [24–27].

Here, we demonstrate electrostatic control over a Mott metal-insulator-transition (MIT) in a single-layer 2D kagome MOF, in excellent agreement with theoretical predictions.

Results and Discussion

A 2D metal-organic framework on an atomically thin insulator

We synthesised the MOF – consisting of 9,10-dicyanoanthracene (DCA) molecules coordinated to copper (Cu) atoms – on monolayer hexagonal boron nitride (hBN) on Cu(111) (see Methods for sample preparation). A scanning tunnelling microscopy (STM) image of a crystalline MOF domain grown seamlessly across the hBN/Cu(111) substrate is shown in Fig. 1a. The long-range modulation of the MOF STM apparent height follows the hBN/Cu(111) moiré pattern, which arises due to mismatch between the hBN and Cu(111) lattices (giving rise to ‘pore’, P, and ‘wire’, W, regions – see upper inset) [28–30].

The MOF is characterised by a hexagonal lattice (lattice constant: 2.01 ± 0.06 nm), with a unit cell including two Cu atoms (honeycomb arrangement; bright protrusions in Fig. 1b) and three DCA molecules (kagome arrangement, with protrusions at both ends of anthracene backbone in Fig. 1b), similar to previous reports [26, 31–33].

We calculated the bandstructure of this DCA_3Cu_2 MOF on hBN/Cu(111) by density functional theory (DFT; with $U = 0$); Fig. 1d. Projection of the Kohn-Sham wavefunctions onto MOF states shows the prototypical kagome energy dispersion with two Dirac bands and a flat band, consistent with prior theoretical calculations for the freestanding MOF [19, 24, 34]. This near-Fermi bandstructure has predominantly molecular DCA character, and is well described by a nearest-neighbour tight-binding (TB) model (see corresponding density of electronic states, DOS, as a function of energy E in Fig. 1e [34]). The hBN monolayer, a 2D insulator with a bandgap > 5 eV [30], prevents electronic hybridization between the underlying Cu(111) surface and the 2D MOF [30]. This allows the MOF to preserve its intrinsic electronic properties, in contrast to previous findings on metal surfaces [26, 33–35]. These $U = 0$ calculations predict that the MOF on hBN/Cu(111) is metallic, with some electron transfer from substrate to MOF leading to the chemical potential lying above the Dirac (charge neutrality) point, close to half-filling of the three kagome bands (Fig. 1d).

Strong electronic interactions have been theoretically predicted in DCA_3Cu_2 [24], and a signature was recently detected experimentally [26]. We therefore calculated the many-body spectral function $A(E)$ – analogous to the DOS in the non-interacting regime – of the free-standing MOF via dynamical mean-field theory (DMFT). In contrast to the TB model or DFT, DMFT explicitly captures electronic correlations caused by the Hubbard energy U (see Methods) [36]. Fig. 1e shows $A(E)$ for $U = 0.65$ eV (consistent with previous experimental estimates [31]) and for a chemical potential which matches the

DFT-predicted occupation of the kagome bands for the MOF on hBN/Cu(111) (see Fig. S1 for further DMFT calculations). We observe two broad peaks (lower and upper Hubbard bands) separated by an energy gap of ~ 200 meV, dramatically different from the non-interacting kagome DOS, and indicative of a Mott insulating phase [24, 37].

Observation of ~ 200 meV Mott energy gap

To experimentally probe the electronic properties of $\text{DCA}_3\text{Cu}_2/\text{hBN}/\text{Cu}(111)$, we conducted differential conductance (dI/dV) scanning tunnelling spectroscopy (STS); dI/dV is an approximation of the local DOS ($A(E)$) in the non-interacting (interacting, respectively) picture. We performed STS at the ends of the DCA anthracene moiety and at the Cu sites of the MOF – locations where we expect the strongest signature of the kagome bands based on the spatial distribution of the orbitals that give rise to these bands [26, 31, 32]. These spectra (Fig. 2a), taken at a pore region of the hBN/Cu(111) moiré pattern, both show broad peaks at bias voltages $V_b \approx -0.2$ and 0.2 V. In a bias voltage window of ~ 0.2 V around the chemical potential E_F ($V_b = 0$), the dI/dV signal is low, significantly smaller than that for bare hBN/Cu(111).

STM images acquired within this low- dI/dV bias voltage window (Fig. 2b, c) show mainly the topography of the MOF, with the molecules appearing as ellipses and the Cu atoms as protrusions, with uniform intensity. Outside the low- dI/dV bias voltage window ($|V_b| > 200$ mV), Cu sites and the ends of the DCA anthracene moieties appear as bright protrusions (Fig. 2d, e), similar to the spatial distribution of the electronic orbitals of the DCA_3Cu_2 MOF associated with the near-Fermi kagome bands (right inset of Fig. 2d; see Figs. S7-S8 for more V_b -dependent STM images and dI/dV maps) [26, 31, 32].

This suggests that the dI/dV peaks at $|V_b| \approx 0.2$ V in Fig. 2a are related to intrinsic MOF electronic states near E_F , with the low- dI/dV bias voltage window of ~ 0.2 V around E_F representing an energy gap, E_g , between these states. This is consistent with in-gap topographic STM imaging in Fig. 2b, c [38]. These dI/dV peaks cannot be attributed to inelastic tunnelling (e.g., MOF vibrational modes) as they are not always symmetric about E_F (see Fig. 3). The gap is much larger than that predicted from spin-orbit coupling in such a system [19], and the highly crystalline growth (Fig. 1a) makes a large disorder-related gap unlikely. Furthermore, the gap is inconsistent with DFT and TB calculations (Fig. 1d, e).

The MOF spectra in Fig. 2a strongly resemble the DMFT-calculated spectral function $A(E)$ in Fig. 1e, including an energy gap of the same magnitude between two similar peaks (Fig. S6). This suggests that these dI/dV spectra are hallmarks of a Mott insulator.

Template-induced Mott metal-insulator transition

We further measured dI/dV spectra of the DCA_3Cu_2 MOF across the hBN/Cu(111) moiré pattern (Fig. 3a, b). In Fig. 3e-f, E_g is centred symmetrically about E_F for spectra taken in the middle of a pore region, while those taken closer to the wire region show the gap shifting upwards in energy (lowering the barrier to creation of a hole). We then observe E_g drastically collapse to zero at the centre of the wire region.

The hBN/Cu(111) moiré pattern consists of a modulation of the local work function Φ (with little structural corrugation), where the quantity $\Delta\Phi = \Phi_{\text{wire}} - \Phi_{\text{pore}}$ depends on the period of the moiré superstructure, λ [28–30]. For $\lambda \approx 12.5$ nm, as for the hBN/Cu(111) domain in Fig. 3a, $\Delta\Phi \approx 0.2$ eV (Fig. 3c) [29]. Due to energy level alignment [39–41], this corrugation of Φ affects substrate-to-MOF electron transfer and hence the effective electron filling of the MOF bands, with this filling smaller at wire than pore regions [39, 42]. This is consistent with the effective reduction of the hole creation barrier at the wire relative to the pore in Fig. 3b.

To capture the effect of this moiré-induced modulation of Φ on the MOF electronic properties, we conducted further DMFT calculations. Using $U = 0.65$ eV (the same as Fig. 1e), we calculated $A(E)$ for a range of E_F assuming a uniform system (neglecting the experimental spatial variation of Φ). We considered a sinusoidal variation of E_F , with an amplitude of 0.2 eV, to match the experimental $\Delta\Phi$ for this specific hBN/Cu(111) moiré domain [29, 42] (Fig. 3c; see Methods). The obtained $A(E)$ (Fig. 3d) quantitatively reproduce the experimental spectra in Fig. 3b, including the LHBH and UHBH (Fig. 3e), and the collapse of E_g at the wire region (Fig. 3f). This provides compelling evidence that our DMFT calculations capture the fundamental electronic properties of the 2D DCA_3Cu_2 MOF, hosting Mott insulating ($E_g \approx 200$ meV) and metal-like phases ($E_g = 0$) controllable via electron filling of the MOF.

The DMFT-calculated spectral functions $A(E)$ for the ungapped metal-like phase (for the smallest electron filling corresponding to measurements at the wire region; Fig. 3c) show peaks near E_F (Fig. 3d) which were not observed experimentally. These peaks are indicative of coherent quasiparticles [36], with their width associated with the quasiparticle lifetime and quasiparticle mean free path ℓ . Via our DMFT and TB calculations (supplementary section S2), we estimate $\ell \approx 10$ nm, much larger than the wire region width of ~ 4 nm. We hypothesize that the coherence peaks are suppressed in the experiment as quasiparticles are strongly scattered by the pore regions (where the MOF remains insulating).

Tip-induced Mott metal-insulator transition

We also performed dI/dV STS of the MOF as a function of tip-sample distance $\Delta z + z_0$ (where z_0 is set by tunnelling parameters), at the centre of a wire region (Fig. 4d; see Fig. S13 for pore). The spectra feature a peak (purple circles in Fig. 4d; sharper than band features in Fig. 3b) whose energy position

increases linearly (Fig. 4e) with increasing Δz . Conversely, the energy position of a subtler band edge (red squares) decreases with increasing Δz , non-linearly and at a lower rate (Fig. 4e). These features cross the Fermi level for the same intermediate Δz , as the spectrum becomes gapless ($E_g = 0$).

As V_b is applied between the tip and Cu substrate, the STM double-barrier tunnel junction (DBTJ) – where the vacuum between tip and MOF is a first tunnel barrier and the insulating hBN is a second one – results in a voltage drop at the MOF location. This can lead to energy shifts of MOF states and/or charging of such states when they become resonant with the Cu(111) Fermi level (Fig. 4a) [31, 41, 43]. In this scenario, the bias voltages corresponding to an intrinsic electronic state, V_{state} , and to charging of such a state, V_{charge} , vary as a function of Δz as:

$$V_{\text{state}}(\Delta z) = \frac{d_{\text{eff}}(V_\infty + \Delta\Phi_{ts})}{(\Delta z + z_0)} + V_\infty, \quad (1)$$

$$V_{\text{charge}}(\Delta z) = -\frac{V_\infty(\Delta z + z_0)}{d_{\text{eff}}} - (V_\infty + \Delta\Phi_{ts}), \quad (2)$$

where d_{eff} is the effective width of the hBN tunnel barrier, V_∞ is the bias voltage corresponding to the electronic state as $\Delta z \rightarrow \infty$, and $\Delta\Phi_{ts}$ is the difference between tip and sample work functions [43].

We fit the Δz -dependent bias voltage associated with the subtle band edge (red squares) in Fig. 4d with Eq. (1), and the bias voltage associated with the sharp peak (purple circles) with Eq. (2) (Fig. 4e). The agreement between experimental data and fits indicate that the subtle spectral band edge (red) represents an intrinsic MOF electronic state, with its energy shifting as Δz varies, and with the sharp peak (purple) corresponding to charging of such a state.

We interpret these results as follows. At the wire site, for large Δz (Fig. 4c), the MOF electronic states are strongly pinned to the substrate, and the MOF near-Fermi kagome bands are approximately half-filled. Here, the MOF is in a Mott insulating phase with a correlated energy gap (bottom spectra of Fig. 4d), with the top of the lower Hubbard band susceptible to charging (as V_b becomes more positive). As Δz decreases gradually to intermediate values (Fig. 4b), the MOF states become less pinned to the substrate, and the difference between tip (Φ_{tip}) and local sample (Φ_{wire}) work functions (with $\Phi_{\text{tip}} > \Phi_{\text{wire}}$; see supplementary section S10) leads to an electron filling of the near-Fermi MOF bands smaller than half-filling. Here, the Mott energy gap collapses and the MOF is in a metallic phase, as shown by the increase in Fermi level dI/dV signal (for $V_b = 0$; Fig. 4f and Figs. S1, S14). As Δz further diminishes (Fig. 4a), the near-Fermi MOF states become more pinned to the tip and depopulate, becoming susceptible to charging (as V_b becomes more negative). Here, the MOF is a trivial insulator (top spectra of Fig. 4d). The STM tip, via V_b and Δz , acts as an electrostatic gate that switches the 2D MOF from Mott insulator to metal to trivial insulator (Fig. S12).

The electrostatic effect of the tip at the wire region is highly localised. Whether the injected holes are truly delocalised in an extended metallic phase

remains an open question, requiring further investigations (e.g., transport experiments).

The spectra for large Δz in Fig. 4d – when the influence of the tip on the system is minimised – suggest that, even at the wire region, the MOF is intrinsically in a Mott insulating phase, unlike what is shown in Fig. 3. In the latter, the MOF is in a gapless phase at the wire site, as E_F is below half-filling due to the combination of a large Φ_{wire} (in comparison with Φ_{pore}) and an intermediate $\Delta z + z_0$ (supplementary section S3).

Conclusion

We have demonstrated that single-layer DCA_3Cu_2 not only hosts a robust Mott insulating phase (with $E_g \gg k_B T$ at $T = 300$ K), but also that Mott MITs can be achieved via template- (Fig. 3) and tip- (Fig. 4) induced gating, quantitatively consistent with DMFT and the DBTJ model. This shows that such phase transitions can be controlled via electrostatic tuning of the chemical potential.

Monolayer DCA_3Cu_2 has been studied on other substrates [26, 31–33, 35], without observing a Mott phase. In our case, the combination of the wide bandgap hBN as a template (allowing the MOF to retain its intrinsic electronic properties), and of the adequate energy level alignment given by the hBN/Cu(111) substrate (resulting in half-filling of kagome bands; Fig. 1d), plays a key role in the realisation of the correlated-electron Mott phase.

Our findings represent a promising step toward incorporation of 2D MOFs as active materials in device-like architectures (e.g., van der Waals heterostructures based on 2D materials), benefiting from efficient synthesis approaches and versatility offered by MOFs, and allowing for access and control of correlated-electron phases therein via electrostatic gating [44]. Our work establishes single-layer 2D MOFs – with crystal geometries allowing for flat bands – as promising platforms for controllable switching between diverse many-body quantum phenomena, potentially including correlated magnetism, superconductivity, and QSLs.

References

- [1] Nakata, Y. *et al.* Monolayer 1T-NbSe₂ as a Mott insulator. *NPG Asia Mater* **8** (11), e321–e321 (2016) .
- [2] Liu, M. *et al.* Monolayer 1T-NbSe₂ as a 2D-correlated magnetic insulator. *Science Advances* **7** (47), eabi6339 (2021) .
- [3] Lin, H. *et al.* Scanning tunneling spectroscopic study of monolayer 1T-TaS₂ and 1T-TaSe₂. *Nano Res.* **13** (1), 133–137 (2020) .
- [4] Chen, Y. *et al.* Strong correlations and orbital texture in single-layer 1T-TaSe₂. *Nat. Phys.* **16** (2), 218–224 (2020) .

- [5] Ruan, W. *et al.* Evidence for quantum spin liquid behaviour in single-layer 1T-TaSe₂ from scanning tunnelling microscopy. *Nat. Phys.* **17** (10), 1154–1161 (2021) .
- [6] Chen, Y. *et al.* Evidence for a spinon Kondo effect in cobalt atoms on single-layer 1T-TaSe₂. *Nat. Phys.* **18** (11), 1335–1340 (2022) .
- [7] Cao, Y. *et al.* Unconventional superconductivity in magic-angle graphene superlattices. *Nature* **556** (7699), 43–50 (2018) .
- [8] Park, J. M., Cao, Y., Watanabe, K., Taniguchi, T. & Jarillo-Herrero, P. Tunable strongly coupled superconductivity in magic-angle twisted trilayer graphene. *Nature* **590** (7845), 249–255 (2021) .
- [9] Zheng, L. *et al.* Emergent charge order in pressurized kagome superconductor CsV₃Sb₅. *Nature* **611** (7937), 682–687 (2022) .
- [10] Ye, L. *et al.* Massive Dirac fermions in a ferromagnetic kagome metal. *Nature* **555** (7698), 638–642 (2018) .
- [11] Yin, J.-X. *et al.* Quantum-limit Chern topological magnetism in TbMn₆Sn₆. *Nature* **583** (7817), 533–536 (2020) .
- [12] Powell, B. J. & McKenzie, R. H. Quantum frustration in organic Mott insulators: from spin liquids to unconventional superconductors. *Rep. Prog. Phys.* **74** (5), 056501 (2011) .
- [13] Kanoda, K. & Kato, R. Mott Physics in Organic Conductors with Triangular Lattices. *Annual Review of Condensed Matter Physics* **2** (1), 167–188 (2011) .
- [14] Miksch, B. *et al.* Gapped magnetic ground state in quantum spin liquid candidate k-(BEDT-TTF)₂Cu₂(CN)₃. *Science* **372** (6539), 276–279 (2021) .
- [15] Shao, Z., Cao, X., Luo, H. & Jin, P. Recent progress in the phase-transition mechanism and modulation of vanadium dioxide materials. *NPG Asia Mater* **10** (7), 581–605 (2018) .
- [16] Balents, L., Dean, C. R., Efetov, D. K. & Young, A. F. Superconductivity and strong correlations in moiré flat bands. *Nat. Phys.* **16** (7), 725–733 (2020) .
- [17] Neupert, T., Denner, M. M., Yin, J.-X., Thomale, R. & Hasan, M. Z. Charge order and superconductivity in kagome materials. *Nat. Phys.* **18** (2), 137–143 (2022) .

- [18] Cui, Y. *et al.* Metal–Organic Frameworks as Platforms for Functional Materials. *Acc. Chem. Res.* **49** (3), 483–493 (2016) .
- [19] Zhang, L. Z. *et al.* Intrinsic Two-Dimensional Organic Topological Insulators in Metal–Dicyanoanthracene Lattices. *Nano Lett.* **16** (3), 2072–2075 (2016) .
- [20] Jin, Y. *et al.* Large-gap quantum anomalous Hall phase in hexagonal organometallic frameworks. *Phys. Rev. B* **98** (24), 245127 (2018) .
- [21] Jiang, W., Ni, X. & Liu, F. Exotic Topological Bands and Quantum States in Metal–Organic and Covalent–Organic Frameworks. *Acc. Chem. Res.* **54** (2), 416–426 (2021) .
- [22] Yamada, M. G., Fujita, H. & Oshikawa, M. Designing Kitaev Spin Liquids in Metal-Organic Frameworks. *Phys. Rev. Lett.* **119** (5), 057202 (2017) .
- [23] Zhang, L.-C. *et al.* Two-dimensional magnetic metal–organic frameworks with the Shastry–Sutherland lattice. *Chem. Sci.* **10** (44), 10381–10387 (2019) .
- [24] Fuchs, M. *et al.* Kagome metal-organic frameworks as a platform for strongly correlated electrons. *J. Phys. Mater.* **3** (2), 025001 (2020) .
- [25] Takenaka, T. *et al.* Strongly correlated superconductivity in a copper-based metal-organic framework with a perfect kagome lattice. *Science Advances* **7** (12), eabf3996 (2021) .
- [26] Kumar, D. *et al.* Manifestation of Strongly Correlated Electrons in a 2D Kagome Metal–Organic Framework. *Advanced Functional Materials* **31** (48), 2106474 (2021) .
- [27] Nourse, H. L., McKenzie, R. H. & Powell, B. J. Multiple insulating states due to the interplay of strong correlations and lattice geometry in a single-orbital Hubbard model. *Phys. Rev. B* **103** (8), L081114 (2021) .
- [28] Joshi, S. *et al.* Boron Nitride on Cu(111): An Electronically Corrugated Monolayer. *Nano Lett.* **12** (11), 5821–5828 (2012) .
- [29] Zhang, Q. *et al.* Tuning Band Gap and Work Function Modulations in Monolayer hBN/Cu(111) Heterostructures with Moiré Patterns. *ACS Nano* **12** (9), 9355–9362 (2018) .
- [30] Auwärter, W. Hexagonal boron nitride monolayers on metal supports: Versatile templates for atoms, molecules and nanostructures. *Surface Science Reports* **74** (1), 1–95 (2019) .

- [31] Yan, L. *et al.* Synthesis and Local Probe Gating of a Monolayer Metal–Organic Framework. *Advanced Functional Materials* **31** (22), 2100519 (2021) .
- [32] Yan, L. *et al.* Two-Dimensional Metal–Organic Framework on Superconducting NbSe₂. *ACS Nano* **15** (11), 17813–17819 (2021) .
- [33] Hernández-López, L. *et al.* Searching for kagome multi-bands and edge states in a predicted organic topological insulator. *Nanoscale* **13** (10), 5216–5223 (2021) .
- [34] Field, B., Schiffrin, A. & Medhekar, N. V. Correlation-induced magnetism in substrate-supported 2D metal-organic frameworks. *npj Comput Mater* **8** (1), 1–10 (2022) .
- [35] Pawin, G. *et al.* A Surface Coordination Network Based on Substrate-Derived Metal Adatoms with Local Charge Excess. *Angewandte Chemie International Edition* **47** (44), 8442–8445 (2008) .
- [36] Georges, A., Kotliar, G., Krauth, W. & Rozenberg, M. J. Dynamical mean-field theory of strongly correlated fermion systems and the limit of infinite dimensions. *Rev. Mod. Phys.* **68** (1), 13–125 (1996) .
- [37] Ohashi, T., Kawakami, N. & Tsunetsugu, H. Mott Transition in Kagome Lattice Hubbard Model. *Phys. Rev. Lett.* **97** (6), 066401 (2006) .
- [38] Repp, J., Meyer, G., Stojković, S. M., Gourdon, A. & Joachim, C. Molecules on Insulating Films: Scanning-Tunneling Microscopy Imaging of Individual Molecular Orbitals. *Phys. Rev. Lett.* **94** (2), 026803 (2005) .
- [39] Joshi, S. *et al.* Control of Molecular Organization and Energy Level Alignment by an Electronically Nanopatterned Boron Nitride Template. *ACS Nano* **8** (1), 430–442 (2014) .
- [40] Zimmermann, D. M. *et al.* Self-assembly and spectroscopic fingerprints of photoactive pyrenyl tectons on hBN/Cu(111). *Beilstein J. Nanotechnol.* **11** (1), 1470–1483 (2020) .
- [41] Pörtner, M. *et al.* Charge State Control of F₁₆CoPc on h-BN/Cu(111). *Advanced Materials Interfaces* **7** (15), 2000080 (2020) .
- [42] Kumar, D., Hellerstedt, J., Lowe, B. & Schiffrin, A. Mesoscopic 2D molecular self-assembly on an insulator. *Nanotechnology* **34** (20), 205601 (2023) .
- [43] Kumar, D., Krull, C., Yin, Y., Medhekar, N. V. & Schiffrin, A. Electric Field Control of Molecular Charge State in a Single-Component 2D

- Organic Nanoarray. *ACS Nano* **13** (10), 11882–11890 (2019) .
- [44] Riss, A. *et al.* Imaging and Tuning Molecular Levels at the Surface of a Gated Graphene Device. *ACS Nano* **8** (6), 5395–5401 (2014) .
- [45] Kresse, G. & Furthmüller, J. Efficiency of ab-initio total energy calculations for metals and semiconductors using a plane-wave basis set. *Computational Materials Science* **6** (1), 15–50 (1996) .
- [46] Perdew, J. P., Burke, K. & Ernzerhof, M. Generalized Gradient Approximation Made Simple. *Phys. Rev. Lett.* **77** (18), 3865–3868 (1996) .
- [47] Blöchl, P. E. Projector augmented-wave method. *Phys. Rev. B* **50** (24), 17953–17979 (1994) .
- [48] Kresse, G. & Joubert, D. From ultrasoft pseudopotentials to the projector augmented-wave method. *Phys. Rev. B* **59** (3), 1758–1775 (1999) .
- [49] Grimme, S., Antony, J., Ehrlich, S. & Krieg, H. A consistent and accurate ab initio parametrization of density functional dispersion correction (DFT-D) for the 94 elements H-Pu. *J. Chem. Phys.* **132** (15), 154104 (2010) .
- [50] Rumble, J. R. *CRC Handbook of Chemistry and Physics* 100 edn (CRC Press/Taylor & Francis, Boca Raton, FL, 2019).
- [51] Schwarz, M. *et al.* Corrugation in the Weakly Interacting Hexagonal-BN/Cu(111) System: Structure Determination by Combining Noncontact Atomic Force Microscopy and X-ray Standing Waves. *ACS Nano* **11** (9), 9151–9161 (2017) .
- [52] Georges, A. & Kotliar, G. Hubbard model in infinite dimensions. *Phys. Rev. B* **45** (12), 6479–6483 (1992) .
- [53] Georges, A. Strongly Correlated Electron Materials: Dynamical Mean-Field Theory and Electronic Structure. *AIP Conference Proceedings* **715** (1), 3–74 (2004) .
- [54] Parcollet, O. *et al.* TRIQS: A toolbox for research on interacting quantum systems. *Computer Physics Communications* **196**, 398–415 (2015) .
- [55] Seth, P., Krivenko, I., Ferrero, M. & Parcollet, O. TRIQS/CTHYB: A continuous-time quantum Monte Carlo hybridisation expansion solver for quantum impurity problems. *Computer Physics Communications* **200**, 274–284 (2016) .

- [56] Gull, E. *et al.* Continuous-time Monte Carlo methods for quantum impurity models. *Rev. Mod. Phys.* **83** (2), 349–404 (2011) .
- [57] Kraberger, G. J., Triebel, R., Zingl, M. & Aichhorn, M. Maximum entropy formalism for the analytic continuation of matrix-valued Green's functions. *Phys. Rev. B* **96** (15), 155128 (2017) .
- [58] Bergeron, D. & Tremblay, A.-M. S. Algorithms for optimized maximum entropy and diagnostic tools for analytic continuation. *Phys. Rev. E* **94** (2), 023303 (2016) .

Methods

Sample preparation

The monolayer DCA_3Cu_2 kagome MOF was synthesised on hBN/Cu(111) in UHV (base pressure $\sim 2 \times 10^{-10}$ mbar). The Cu(111) surface was first cleaned via 2-3 cycles of sputtering with Ar^+ ions and subsequent annealing at ~ 770 K. A hBN monolayer was synthesised on Cu(111) via the thermal decomposition of borazine [30]. We dosed a partial pressure of borazine of $\sim 9 \times 10^{-7}$ mbar for 45 minutes with the Cu(111) sample maintained at 1140 K. We kept the Cu(111) sample at this temperature for a further 20 minutes to ensure a complete reaction. We then cooled the sample to room temperature and deposited the DCA molecules via sublimation at 390 K, corresponding to a deposition rate of 0.007 ML/sec. In our experiments we considered DCA coverages of $\sim 0.4\text{--}0.6$ ML. We then further cooled the sample to ~ 77 K before depositing Cu via sublimation at 1250 K (Cu deposition rate: ~ 0.002 ML/sec; typical Cu coverages in our experiments: ~ 0.05 ML). Finally, the sample was annealed to ~ 200 K for 15 minutes. Further details in supplementary section S4.

The DCA_3Cu_2 MOF crystalline structure was found to be commensurate with the hBN lattice but incommensurate with the long-range hBN/Cu(111) moiré patterns of different sizes, across which the MOF grows without disruption (see Fig. S5). The hBN/Cu(111) moiré pattern is clearly visible in large-scale STM images of the MOF (Fig. 1a). This is consistent with the modulation of the MOF's electronic properties illustrated in Fig. 3 (also see dI/dV maps in Fig. S8).

STM and STS measurements

All STM and dI/dV STS measurements were performed at 4.5 K (base pressure $< 1 \times 10^{-10}$ mbar) with a hand-cut Pt/Ir tip. All STM images were acquired in constant-current mode with tunnelling parameters as reported in the text (bias voltage applied to sample). All dI/dV spectra were obtained by acquiring $I(V)$ at a constant tip-sample distance (stabilised by a specified setpoint tunnelling current and bias voltage), and by then numerically differentiating $I(V)$ to obtain dI/dV as a function of bias voltage. Tips were

characterised on regions of bare hBN/Cu(111) prior to spectroscopy measurements, where the Shockley surface state of Cu(111) could be observed (grey curve in Fig. 2a, onset shifted upwards in energy due to confinement by hBN monolayer) [28].

DFT calculations

We calculated the non-spin-polarised band structure of DCA_3Cu_2 on hBN on Cu(111) via DFT (Fig. 1d), using the Vienna Ab-Initio Simulation Package (VASP) [45] with the Perdew-Burke-Ernzerhof (PBE) functional under the generalised gradient approximation [46]. We used projector augmented wave (PAW) pseudopotentials [47, 48] to describe core electrons, and the semi-empirical potential DFT-D3 [49] to describe van der Waals forces.

The substrate was modelled as three Cu atoms thick, with the bottom layer fixed at the bulk lattice constant [50]. A layer of passivating hydrogen atoms was applied to the bottom face to terminate dangling bonds.

A 400 eV cut-off was used for the plane wave basis set. The threshold for energy convergence was 10^{-4} eV. The atomic positions of the $\text{DCA}_3\text{Cu}_2/\text{hBN}/\text{Cu}(111)$ were relaxed until Hellmann-Feynman forces were less than 0.01 eV/Å, using a $3 \times 3 \times 1$ k-point grid for sampling the Brillouin zone and 1st order Methfessel-Paxton smearing of 0.2 eV. The charge density for the relaxed structure was calculated using an $11 \times 11 \times 1$ k-point grid, Blochl tetrahedron interpolation, and dipole corrections. The band structure was determined non-self-consistently from the charge density.

Note that small (< 1 Å) perturbations in the height of DCA_3Cu_2 above the hBN/Cu(111) do not appreciably affect the calculated band structure. As such, small perturbations in height related to the hBN/Cu(111) moiré pattern (of at most 0.7 Å [51]) were not captured by these calculations [34].

DMFT calculations

We performed dynamical mean-field theory (DMFT) calculations on the free-standing DCA_3Cu_2 kagome MOF. We used the Hubbard model for a kagome lattice with nearest-neighbour hopping,

$$H = -t \sum_{\langle i,j \rangle, \sigma} \hat{c}_{i,\sigma}^\dagger \hat{c}_{j,\sigma} + U \sum_i \hat{n}_{i,\uparrow} \hat{n}_{i,\downarrow}, \quad (3)$$

where the first term is the tight-binding (TB) Hamiltonian with nearest-neighbour hopping energy t , $\sum_{\langle i,j \rangle}$ is a sum over nearest-neighbour sites, and the second term is the interaction Hamiltonian with on-site Coulomb repulsion U . The operator $\hat{c}_{i,\sigma}^\dagger$ ($\hat{c}_{i,\sigma}$) creates (annihilates) an electron at site i with spin σ ; $\hat{n}_{i,\sigma} = \hat{c}_{i,\sigma}^\dagger \hat{c}_{i,\sigma}$ is the density operator. We take $t = 0.05$ eV to match prior DFT calculations of DCA_3Cu_2 [19, 24, 34].

We first calculated the non-interacting ($U = 0$) density of states (DOS; blue curve in Fig. 1e) by numerically integrating over all momenta in the

first Brillouin zone. The chemical potential E_F in Fig. 1e was chosen to be consistent with the electron filling predicted by DFT in Fig. 1d. We applied a thermal broadening ($k_B T = 2.5$ meV) to this non-interacting TB DOS to make it consistent with the thermal broadening of the DMFT-generated (see below) spectral function $A(E)$ in Fig. 1e.

To account for electronic correlations, we then implemented a DMFT formalism [36, 52, 53] using the Toolbox for Researching Interacting Quantum Systems (TRIQS) [54], with the continuous-time hybridization expansion solver (CTHYB) [55, 56] at a temperature of ~ 29 K ($k_B T \approx 0.05t$), with $U = 0.65$ eV. To use a single-site DMFT formalism [36] with the kagome band structure, the non-interacting DOS of the three kagome bands were combined into a single function for use as the input into the DMFT procedure.

We calculated the many-body spectral functions $A(E)$ (analogous to the DOS, but in the interacting regime; Fig. 3d) via analytic continuation using the maximum entropy method (MaxEnt) as implemented in TRIQS [57]. The meta-parameter, α , was determined from the maximum curvature of the distance between the MaxEnt fit and data, χ^2 , as a function of α [58].

Each DMFT calculation assumed a spatially uniform work function Φ ; long-range modulation of Φ is beyond the capabilities of DMFT. As such, the spatially varying sample work function Φ resulting from the experimental hBN/Cu(111) moiré pattern was not explicitly captured in the individual $A(E)$ spectra in Fig. 3d. This spatial variation of Φ was approximated by varying the uniform E_F of the system for each individual $A(E)$ spectrum. Each of these $A(E)$ spectra was then associated to a specific location of the hBN/Cu(111) moiré pattern (and hence to a specific experimental dI/dV curve) based on how this variation of E_F would translate to a local Φ . These calculations assume that the theoretical $A(E)$ spectra, calculated with a uniform E_F (and hence uniform Φ , omitting effects of non-locality), are reasonable representations of the locally acquired experimental dI/dV curves, which are affected by a spatially varying Φ . While this assumption of locality is reasonable for the insulating phase (i.e., localised states), long electronic coherence lengths may lead to discrepancies between theory and experiment in the metallic phase at the ‘wire’ region (see Figs. 3, 4), as discussed in the main text and supplementary section S2.

All codes relating to DMFT and MaxEnt are available at <https://doi.org/10.5281/zenodo.7439858>.

DBTJ model

In Figs. 4d, e, the bias voltage, V_{state} (red squares), corresponds to the energy level of an intrinsic MOF frontier electronic state (which is susceptible to charging), at a band edge in either the Mott or trivial insulator regime (see supplementary section S8). The bias voltage, V_{charge} (purple circles), corresponding to the charging peak associated with such MOF state, is given by a local maximum in dI/dV .

In Fig. 4e, we considered four experimental datasets for fitting with Eqs. (1) and (2): $V_{\text{state}}(\Delta z)$ (red squares) and $V_{\text{charge}}(\Delta z)$ (purple circles) for small values of Δz (trivial insulator phase), and $V_{\text{state}}(\Delta z)$ and $V_{\text{charge}}(\Delta z)$ for large values of Δz (Mott insulator phase). Given the Mott MIT, we considered two different intrinsic MOF band edges susceptible of charging, embodied in two different values of V_∞ : one for the trivial insulator phase (small values of Δz) and one for the Mott insulator phase (large Δz). This phase transition is evident from the offset in V_{state} (red squares in Fig. 4e) observed when Δz varies from small to large (through the metallic phase at intermediate Δz). Accordingly, we used a global fitting approach to obtain the same fitting parameters d_{eff} , z_0 , and $\Delta\Phi_{\text{ts}}$ (characteristic of the DBTJ and the acquisition location) for these four experimental datasets, and a separate V_∞ value for each regime.

Acknowledgements

A.S. acknowledges funding support from the ARC Future Fellowship scheme (FT150100426). B.J.P. acknowledges funding support from the ARC Discovery Project scheme (DP180101483). H.L.N. acknowledges funding support from the MEXT Quantum Leap Flagship Program (JPMXS0118069605). B.L., J.H., J.C., and N.V.M. acknowledge funding support from the Australian Research Council (ARC) Centre of Excellence in Future Low-Energy Electronics Technologies (CE170100039). B.L., B.F., and J.C. are supported through Australian Government Research Training Program (RTP) Scholarships. B.F. and N.V.M. gratefully acknowledge the computational support from National Computing Infrastructure and Pawsey Supercomputing Facility. The authors also thank Prof. Michael S. Fuhrer, Prof. Jaime Merino Troncoso, and Dr. Daniel Moreno Cerrada for valuable discussions.

Author Contributions

B.L., J.H., and A.S. conceived and designed the experiments. B.L., J.H., and J.C. performed the experiments. B.F. and H.L.N. performed the theoretical calculations with guidance from B.J.P. and N.V.M. All authors contributed to writing the manuscript.

Competing Interests

The authors declare no competing interests.

Additional Information

Supplementary Information

Further DMFT calculations; discussion of quasiparticle peaks in Fig. 3; MOF growth and structure details; comparison between DMFT and STS; bias dependent STM topography images and dI/dV maps; method for determining band edges; further charging signatures; estimate of tip work function; further DBTJ details; $dI/dV(\Delta z)$ measurements at the pore region; further evidence of metallic character.

Correspondence & Requests for Materials

To be addressed to Ben J. Powell, Nikhil V. Medhekar, or Agustin Schiffrin.

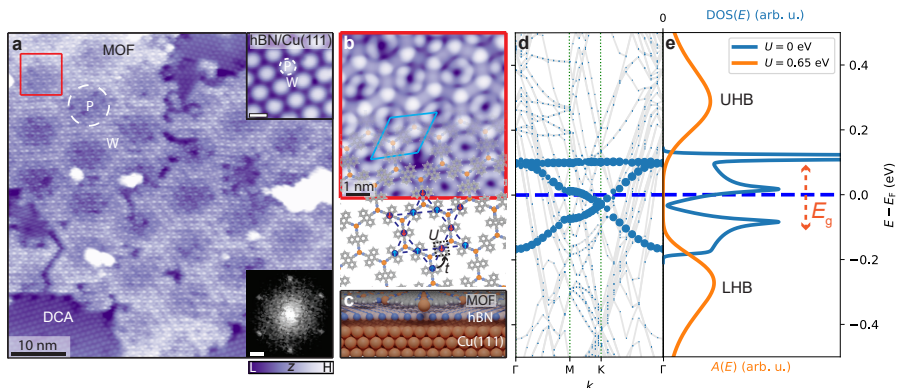


Fig. 1 A 2D kagome MOF on an atomically thin insulator: DCA_3Cu_2 on single-layer hBN on Cu(111). **a**, STM image of MOF (with organic DCA-only regions; $V_b = -1$ V, $I_t = 10$ pA). ‘P’ and ‘W’ indicate pore (dashed white circle) and wire regions of hBN/Cu(111) moiré pattern. Lower inset: Fourier transform of STM image; sharp spots correspond to MOF hexagonal periodicity (scale bar: 0.25 nm $^{-1}$). Upper inset: STM image of bare hBN/Cu(111) moiré pattern ($V_b = 4$ V, $I_t = 100$ pA, scale bar: 4 nm). **b**, Top-view of MOF model overlaid upon small-scale STM image of region within red box in (a) ($V_b = -1$ V, $I_t = 10$ pA). MOF unit cell indicated in light blue. Blue dashed lines and solid circles: kagome pattern formed by DCA molecules, with inter-site electron hopping, t , and on-site Coulomb repulsion, U . **c**, Model of MOF/hBN/Cu(111) (side view). Hydrogen: white; carbon: grey; boron: pink; nitrogen: blue; copper: orange. **d**, Electronic bandstructure calculated by DFT (with $U = 0$) [34]. Blue circles: projections onto MOF states. Grey curves: Cu(111) states (hBN states do not contribute within the shown energy range). Hybridisation between MOF and Cu(111) is hindered by the hBN monolayer; the MOF bandstructure retains its kagome character. Chemical potential E_F (blue dashed line) is close to half-filling of kagome bands. **e**, Density of states, $\text{DOS}(E)$ (tight-binding model with thermal broadening, $U = 0$, blue), and spectral function, $A(E)$ (DMFT, $U = 0.65$ eV, orange), of free-standing MOF. Local Coulomb interaction opens a significant Mott energy gap E_g between lower (LHB) and upper Hubbard bands (UHB).

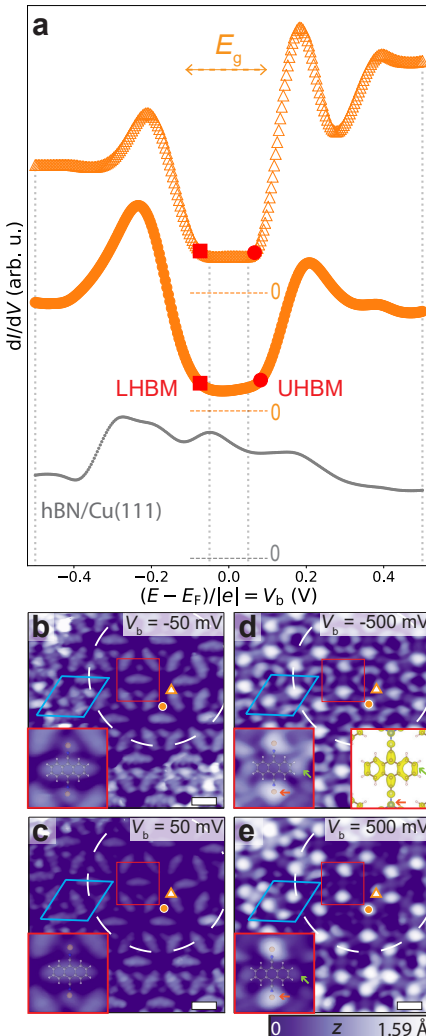


Fig. 2 Bandgap $E_g \approx 200$ meV in DCA₃Cu₂ MOF on hBN/Cu(111). **a**, dI/dV spectra at MOF positions indicated by orange markers in (b-e) and on bare hBN/Cu(111) (grey dots) (setpoint: $V_b = -500$ mV, $I_t = 500$ pA). Gray dotted vertical lines indicate bias voltages at which STM images were acquired in (b-e). Spectra offset for clarity. Dashed horizontal lines indicate $dI/dV = 0$ reference for each curve. Spectra reveal a bandgap $E_g \approx 200$ meV. The non-zero dI/dV within gap is due to states of underlying Cu(111) leaking through hBN. Red squares (circles): lower Hubbard band maxima, LHBMs (upper Hubbard band minima, UHBMs). **b-e**, STM images of MOF on hBN/Cu(111) at specified bias voltages ($I_t = 10$ pA). White dashed circle: hBN/Cu(111) moiré pore. MOF unit cell indicated in light blue. Scale bars: 1 nm. Insets: zoom-in of region within red box, with overlaid Cu-DCA-Cu chemical structure, showing significant contributions from the ends of the DCA anthracene moiety (green arrow) and Cu (orange arrow) for $V_b <$ LHBMs and $V_b >$ UHBMs. Right inset in (d): charge density isosurface ($0.0025 \text{ e}^{-\text{\AA}^{-3}}$) of DCA₃Cu₂ obtained by integration of near-Fermi (± 0.5 eV) DFT wavefunctions.

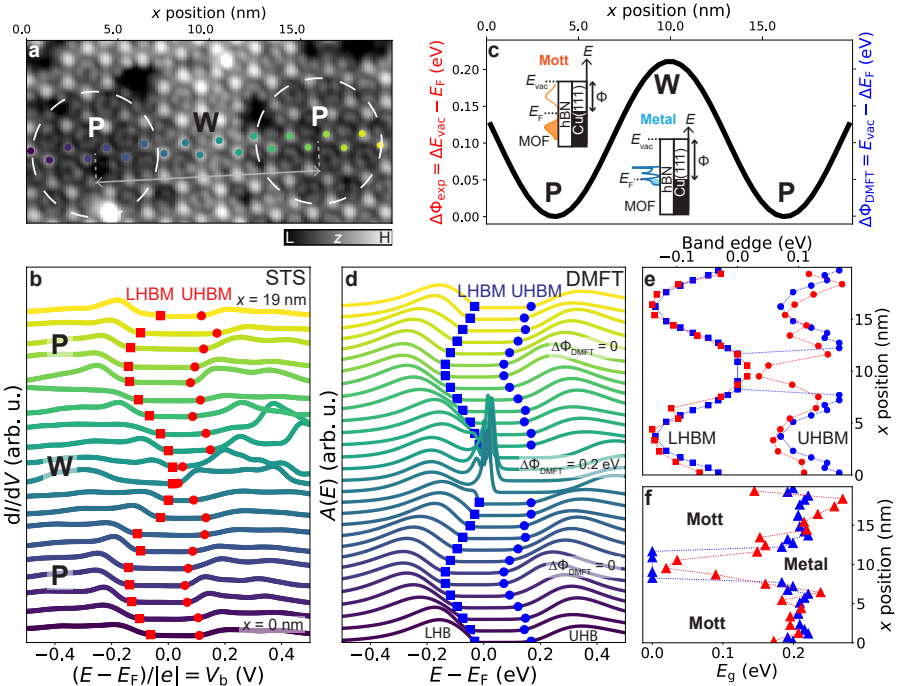


Fig. 3 Variation of Mott energy gap in DCA_3Cu_2 MOF induced by hBN/Cu(111) moiré modulation of local work function. **a**, STM image of MOF ($V_b = -1$ V, $I_t = 10$ pA). White dashed circles (P): hBN/Cu(111) moiré pores, separated by wire (W). Grey arrow indicates moiré period $\lambda \approx 12.5$ nm. **b**, dI/dV spectra acquired at MOF Cu sites, at positions indicated by coloured markers in (a) (tip 190 pm further from STM setpoint $V_b = 10$ mV, $I_t = 10$ pA). Energy gap $E_g \approx 200$ meV at P regions, vanishing at W region (LHBM: lower Hubbard band maximum; UHBM: upper Hubbard band minimum). **c**, Sinusoidal variation of work function, $\Delta\Phi = \Delta E_{\text{vac}} - E_F$ (E_{vac} : vacuum energy level), across hBN/Cu(111) moiré domain with periodicity $\lambda \approx 12.5$ nm [29], affecting the MOF electron filling. **d**, Spectral functions $A(E)$ calculated via DMFT ($U = 0.65$ eV, $t = 0.05$ eV) for isolated uniform DCA_3Cu_2 , for different values of E_F . We account for experimental corrugation $\Delta\Phi$ by varying E_F sinusoidally with an amplitude of 0.2 eV as per (c) (see Methods). **e**, **f**, Experimental (red; from c) and DMFT (blue; from d) LHBM (squares), UHBM (circles) and energy gap E_g (triangles), as a function of x in (a) (experiment) or corresponding E_F (DMFT).

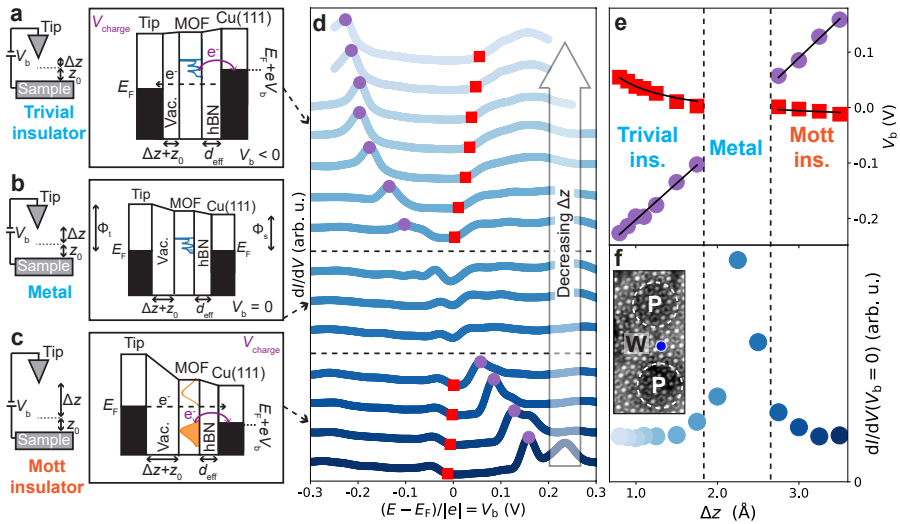


Fig. 4 Mott insulator-to-metal transition controlled via tip-induced gating. **a-c**, Schematics and energy diagrams of tunnelling and charging processes at a double-barrier tunnel junction (DBTJ), consisting of STM tip, vacuum barrier (vac.), MOF, hBN barrier and Cu(111), for small, intermediate and large tip-sample distances ($\Delta z + z_0$). When V_b is applied, voltage drop at MOF location enables tip-controlled charging, energy level shifts and gating of MOF transitions, from (correlated) Mott insulator to metal to trivial insulator. **d**, dI/dV spectra at MOF DCA anthracene end site, at hBN/Cu(111) moiré wire, for different $\Delta z + z_0$ (z_0 given by STM setpoint $V_b = 10$ mV, $I_t = 10$ pA). Purple circles (red squares): MOF charging peak (intrinsic electronic state at MOF band edge). Spectra normalised and offset for clarity. **e**, V_{charge} (purple circles in d) and V_{state} (red squares in d) as a function of Δz . Black solid lines: global fits to Eqs. (1) and (2). **f**, dI/dV signal at Fermi level ($V_b = 0$) as a function of Δz , from (d). Increased $dI/dV(V_b = 0)$ indicates metallic phase at intermediate $\Delta z + z_0$. Inset: STM image of MOF on hBN/Cu(111) showing site (blue marker) where $dI/dV(\Delta z)$ measurements were performed ($V_b = -1$ V, $I_t = 10$ pA).